https://doi.org/10.1016/j.bios.2022.113999

Wavelength-regulated switchable photoelectrochemical system for concurrent detection of dual antibiotics

Ding Jiang,[a,b] Yude Zhang,[a] Xiaojiao Du,[c] Youhua Tan[b], Wen Chen[d], Mo Yang[b,*]

[a] *Jiangsu Key Laboratory of Advanced Catalytic Materials and Technology, School of Petrochemical Engineering, Changzhou University, Changzhou, Jiangsu, 213164, P. R. China*

[b] *Department of Biomedical Engineering, The Hong Kong Polytechnic University, Kowloon 999077, Hong Kong SAR, P. R. China*

[c] *Oakland International Associated Laboratory, School of Photoelectric Engineering, Changzhou Institute of Technology, Changzhou, Jiangsu, 213032, P. R. China*

[d] *Department of Electronic and Information Engineering, The Hong Kong Polytechnic University, Kowloon 999077, Hong Kong SAR, P. R. China*

ABSTRACT

Concurrent detection of antibiotics with high sensitivity and reliability is always of high importance for food safety and environmental monitoring. Herein, a wavelength-dependent photoelectrochemical (PEC) aptasensor based on TiO_2-Ag/nitrogen doped graphene composites (TiO_2-Ag/NDG) was developed for concurrent detection of two antibiotics with signal amplification function. The as-fabricated ternary nanocomposites could concurrently detect two antibiotics using two different aptamer molecules as recognition elements, amplify the photocurrent outputs and perform a photocurrent-switchable operation, where photocurrents could be switched between anodic direction and cathodic direction via simply regulating the irradiation wavelength. Such proposed wavelength-dependent PEC sensing strategy was capable of concurrently detecting chloramphenicol (CAP) with a wide linear detection range from 50 pM ~ 10 nM under irradiation of 380 nm and tetracycline (TET) with a linear detection range from 100 pM to 100 nM under irradiation of 600 nm, respectively. The limits of detection (LOD) for CAP and TET were 16.7 pM and 30 pM, respectively. Moreover, this PEC sensor also displayed good specificity and outstanding reliability in real sample applications. This wavelength-dependent PEC strategy could be conveniently adapted to other applications in food safety biosensing and environmental monitoring,

Keywords: Photoelectrochemical sensing; Antibiotic; TiO_2; Nitrogen-doped graphene composites

1. Introduction

As a hot spot of global concern, the identification and detection of antibiotic pollution is one of the major environmental issues involving human health damage and ecological risks (Martin et al., 2020; Li et al., 2020b; Ye et al., 2017; Brodin et al., 2013). It has been proven that trace amount of antibiotics even below ppb level can also impose a devastating disaster on ecosystem, and then produce superbugs with strong resistance to original antibiotics (Martin et al., 2020). Chloramphenicol (CAP) and tetracycline (TET) are two very common antibiotics used in veterinary medicine, which should be sensitively detected for food safety (Jeong et al., 2010; Song et al., 2020). Therefore, several strict standards have been implemented for the discharge of food or wastewater containing antibiotics (European Union (EU), Commission regulation No. 37/2010, Off. J. Eur. Communities: Legis., 2010). Actually, a single antibiotic test is often not efficient in terms of food safety and environmental protection owing to its limitation (Li et al., 2020a; Joshi et al., 2020). Therefore, concurrent detection of antibiotics with significant advantages such as low cost and high measurement efficiency have undoubtedly attracted widespread attention to meet the growing demand for food safety and environmental protection.

So far, various methods have been applied for sensitive and concurrent detection of multiple targets, including high performance liquid chromatography (Lajin et al., 2020), colorimetry (Zhou et al., 2017), fluorescence (Qian et al., 2020), and photoelectrochemical (PEC) technique (Dai et al., 2016; Wang et al., 2017; Wang et al., 2015). Among these strategies, PEC sensing has gained tremendous popularity owing to its simple operation, rapid response, low cost and high accuracy. Based on the energy conversion from light energy to electric energy, PEC sensing also possesses

the merit of high sensitivity due to the separation of excitation and response signals (Jiang et al., 2021; Jiang et al., 2019; Chu et al., 2020). Wavelength-resolved PEC sensors have been developed for concurrent detection (Wang et al., 2015; Deng et al., 2019). Wang et al. fabricated an ultrasensitive PEC biosensor for detection of multiple biomarkers with the use of light addressing strategy, i.e. to use light irradiation to generate electron-hole pairs at the irradiated position of the semiconductor layer to obtain a photocurrent with exerted bias potential (Wang et al., 2015). Deng et al. developed a wavelength-resolved PEC sensor for concurrent detection of Pb^{2+} and Mg^{2+} by click reaction (Deng et al., 2019). Although concurrent detection of multiple targets has been achieved through these strategies, there are still some limitations that can be further improved. Firstly, these approaches suffer from limited sensitivity because of the complicated fabrication process of the biosensor and tedious signal amplifying strategies. Moreover, all these high-throughput PEC sensors display anodic photocurrent curves under different wavelengths of light, which are prone to produce false positive signals (Wang et al., 2015; Deng et al., 2019). In order to overcome these limitations to improve sensitivity and reliability, it is of great importance to further improve the sensitivity of these PEC multiplex sensors and distinguish the photocurrent signals under different wavelengths of light without complex signal amplifying strategies.

Light-driven PEC logic gates with wavelength-switchable photocurrent have aroused extensive interests, whose photocurrents could be switched from anodic to cathodic direction via simply regulating the irradiation wavelength with ratio-type response to improve sensitivity and reliability (Antuch et al., 2018, Chen et al., 2015b). The development of such logic gate system depends on the design of electrodes based on nanostructured materials. Recently, several

photocurrent-switchable systems based on various nanostructured materials have been developed including sulfide-based nanoplates (Chen et al., 2017), hierarchically structured biphasic ambipolar oxide (Bourée et al., 2016), polymer nanosheets assemblies (Matsui et al., 2004), and TiO_2 nanoparticles incorporated peptide appended perylene bisimide (Loget et al., 2015; Furtado et al., 2006; Szacilowski et al., 2006; Roy et al., 2017). However, these photoactive materials-based logic gates always suffer from low signal transmission efficiency, which limit their analytical accuracy in the actual detection (Jiang et al., 2016). Thus, it is important to design a novel PEC system based on wavelength-switchable photocurrent logic gates with high signal transmission efficiency and good amplification effect.

Herein, we developed a novel PEC system with photocurrent-switching characteristics based on hybrid nanocomposite composed of photoactive TiO_2 nanoparticles, Ag nanoclusters and nitrogen-doped graphene nanosheets (TiO_2-Ag/NDG) for concurrent detection of two antibiotics of CAP and TET. This PEC system showed a wavelength-switchable photocurrent modulation mechanism, whose photocurrents could be switched between anodic direction and cathodic direction via simply regulating the irradiation wavelength. The ratio-type photocurrent response under various light wavelengths could not only increase the sensitivity but also improve the reliability of this sensor. By combining the wavelength-switchable PEC function with various antibiotic aptamers, a PEC aptasensor platform was developed for concurrent detection of CAP and TET with high sensitivity, specificity and reliability. This novel wavelength-switchable PEC sensing system could not only provide a high-performance platform for detection of dual antibiotics, but also have high potential to be applied to other applications including food

surveillance, environmental monitoring and disease diagnosis.

2. Experimental section

2.1. Chemicals

We purchased glycine (Gly), $AgNO_3$, $TiO(C_4H_9O)_4$, HNO_3, Chloramphenicol (CAP), tetracycline (TET), doxycycline, cipro floxacin, kanamycin, neomycin sulfate, and chlortetracycline from Aladdin Reagent Co., Ltd. Graphene oxide (GO) nanosheets were purchased from Nanjing XFNANO Materials Tech Co., Ltd. $TiO(NO_3)_2$ was prepared by dissolving $TiO(C_4H_9O)_4$ in HNO_3 at 10 : 1 by volume ratio. The CAP aptamer and TET aptamer were chosen according to the previous literatures and purchased from Shanghai Sangon Biotech Co. Ltd. with the following sequences (Jiang et al., 2019; Ge et al., 2018):

CAP aptamer: 5′-TGTAATTTGTCTGCAGCGGTTCTTGATCGCTGACACCATATTATGAAGA-3’

TET aptamer: 5′-CGTACGGAATTCGCTAGCCCCCCGGCAGGCCACGGCTTGGGTTGGTCCCACTGCGCGTGGATCCGAGCTCCACGTG-3′

2.2. Preparation of TiO_2-Ag/NDG nanocomposites and TiO_2/NDG nanocomposites

TiO_2-Ag/NDG nanocomposites were prepared through a facile hydrothermal treatment method (Shah et al., 2013; Durango-Giraldo et al., 2019). In a typical procedure, 3 mL graphene oxide (GO) suspension (1 mg/mL) was mixed with $TiO(NO_3)_2$, $AgNO_3$, and Gly at a certain mass

ratio. After sonicating for 10 minutes, the above suspension was transferred into an alumina crucible and was then heated in an evacuated silica tube at 500ºC for 2 h in nitrogen atmosphere. TiO_2/NDG nanocomposites were obtained via the similar method without the addition of $AgNO_3$.

2.3. Electrodes Fabrication

To prepare the TiO_2-Ag/NDG nanocomposites-modified indium tin oxide (ITO) electrodes, 5.0 mg of the TiO_2-Ag/NDG nanocomposites was dispersed in 2.5 mL of ultrapure water, and then ultrasound for several minutes. After that, 40 μL of the suspensions dropped on the surface of ITO substrate (1 cm×0.5 cm), and dried at 60 ºC for 10 h. For comparison, TiO_2/NDG nanocomposites-modified ITO electrodes were prepared following the same procedures.

2.4. Construction of the PEC aptasensor

The PEC aptasensor based on the TiO_2-Ag/NDG nanocomposites was then fabricated for detection of single and multiple antibiotic targets. Compared with antibody-based biosensor, aptamer-based biosensor has the advantages of easier immobilization, better stability, and higher reproducibility (McConnell et al., 2020; Shi et al., 2017). Typically, prior to modification, the sensing area of the ITO electrode was divided into two equal areas (0.5 cm × 1 cm) with insulating rubber tape. 20 μL TiO_2-Ag/NDG nanocomposites suspension were then coated on each independent 0.5 cm^{-2} surface area on the nanocomposites modified ITO electrode, respectively and dried at 60 ºC for 10 h. Subsequently, 20 μL of the CAP aptamer with 1.5 μM concentration was coated on the ITO surface (Sensing area 1), and 20 μL of the TET aptamer (2.0 μM) was coated

on another ITO surface (Sensing area 2). To ensure the effective immobilization of aptamer, the nanocomposites modified ITO electrode was incubated with aptamer solution at room temperature for 12 h. Afterwards, the above ITO electrode was washed by 0.1 M PBS solution to remove the excess non-adsorbed aptamer. In the detection process of PEC sensing, 20 μL solution of targeted antibiotics with different antibiotics concentrations were dropped on the ITO electrodes for 20 min and then washed using 0.1 M PBS solution for the following PEC measurement.

2.5. Photoelectrochemical measurements

Photoelectrochemical measurements were performed using a three electrode setup under illumination with an Ag/AgCl reference electrode and a Pt wire as a counter electrode in 0.1 M phosphate buffered solution (pH = 7.4). The electrochemical behaviour was monitored with a CHI 660E electrochemical workstation (Chenhua, Shanghai). The illumination was provided by a Xe lamp (100 mW/cm^2, CEL-S500, China Education Au-light) with different filters (from 350 nm to 650 nm). Moreover, three samples and sensors were used to acquire the data.

2.6. *Sample pretreatment*

The Yangtze River water was firstly filtered through a 0.22mm filter membrane and the extract was directly used for detection. For honey samples, 1g of honeycomb was chopped in a conventional food processor for 15 min to obtain a well-mixed homogenate. The homogenate was then centrifuged for 20 min at 1000 rpm to remove the solids, and then the supernatant was filtered through a 0.22 μm membrane. Subsequently, the extract was transferred to a 10 mL volumetric

flask and the volume was made up with ethanol. Different concentrations of antibiotics were then spiked into water and honey samples for the PEC sensing.

3. Results and discussion

3.1. Characterizations of TiO_2-Ag/NDG nanocomposites

The phase structure of the as-synthesized TiO_2-Ag/NDG composites was measured by X-ray diffraction (XRD) spectroscopy. As shown in Fig. 1A, the XRD pattern possessed several diffraction peaks from 25.3° to 75.0°, which matched well with the scattering angles of the standard anatase TiO_2 (JCPDS No. 21-1272) (Zhao et al., 2016; Liu et al., 2016a). Moreover, some sharp diffraction peaks at 38°, 44°, 64.5°, and 77.3° could be clearly observed, which corresponded to the cubic Ag crystal (JCPDS No. 65-2871) (Wang et al., 2014; Jiang et al., 2016). Notably, all the diffraction peaks were wide, indicating the size the TiO_2 and Ag was quite small. There was no characteristic diffraction peak of NDG at 26.7° owing to its relatively low content. The compositional analysis and elemental chemical states of TiO_2-Ag/NDG composites were further studied via X-ray photoelectron spectroscopy (XPS). Fig. 1B revealed the full-scan survey spectrum of the TiO_2-Ag/NDG composites with the relevant elements of Ti, Ag, C, N and O. The high-resolution scan of Ti_{2p} in Fig. S1A showed two peaks centered at 459.26 and 464.97 eV, which were fitted with Ti $2p_{3/2}$ and Ti $2p_{1/2}$ spin-orbit splitting states of typical TiO_2 (Zhao et al., 2016; Liu et al., 2016a). Fig. S1B exhibited two well-resolved peaks located at 367.8 and 373.8 eV, corresponding to the binding energy value of Ag(0) (Temerov et al., 2020; Gilea et al., 2018). In

the high resolution spectrum of N_{1s} (Fig. 1C), the broad peak could be deconvoluted into three peaks at 398.6 eV, 399.8 eV and 401.2 eV, which represented pyridine N, pyrrolic N and quaternary N atoms doped in the graphene structure respectively and demonstrated the existence of NDG in the nanocomposite (Jiang et al., 2015; Wu et al., 2012). In addition, the elemental composition of the nanocomposite has been quantified based on the XPS survey spectra in Table S1, which further confirmed the successful fabrication of the TiO_2-Ag/NDG nanocomposites. Therefore, it could be concluded that the hybrid composites were successfully fabricated by conjunction with TiO_2, Ag and NDG. Transmission electron microscopy (TEM) was also performed to further analyze the morphology and structure of the TiO_2-Ag/NDG composites. As shown in Fig. 1D and 1E, TiO_2-Ag/NDG showed quasi-spherical shape with an average size of 4.9±1.4 nm (Fig. S2). Moreover, the representative high-resolution TEM image (Fig. 1F) for TiO_2-Ag/NDG composites exhibited lattice fringes with spacing of 0.351 nm and 0.235 nm, which could be indexed to the (101) plane of anatase TiO_2 and the d-spacing of Ag (111) plane, respectively (Jiang et al., 2016; Wen et al., 2011).

3.2. Wavelength-switchable PEC performance

To explore the interesting wavelength-switchable PEC performance of the as-prepared TiO_2-Ag/NDG composites, the transient-state photocurrent under intermittent illumination with different filter wavelengths were investigated. As shown in Fig. 2A, the photocurrent can be switched by changing wavelength from 350 nm to 650 nm. Under UV light irradiation (< 400 nm), the nanocomposites displayed anodic photocurrent, while under illumination with the wavelengths

longer than 450 nm, cathodic photocurrents were observed. The maximum anodic and cathodic photocurrents were achieved under 380 nm and 600 nm, respectively. Light-driven TiO_2 PEC logic gates with various input wavelengths as inputs to modulate the output photocurrent have been reported (Loget et al., 2015; Furtado et al., 2006; Szacilowski et al., 2006). Our TiO_2-Ag/NDG PEC nanocomposite has a similar XOR logic gate mechanism for output photocurrent modulation through 380 nm and 600 nm light inputs (Scheme S1). Here, only 380 nm excitation (Input: 1-0) or only 600 nm excitation (Input: 0-1) leads to an anodic photocurrent and a cathodic photocurrent, respectively. However, simultaneous excitation of both 380 nm and 600 nm (Input: 1-1) leads to no photocurrent.

It was well known that TiO_2 is an n-type semiconductor, which could only absorb UV light and then produce anodic photocurrent (Chen et al., 2015b; Roy et al., 2017; Zhao et al., 2016). Referring to the previous studies, nitrogen-doped graphene could enhance charge transfer and prolong the lifetime charge carriers (Jiang et al., 2019; Ge et al., 2018; Jiang et al., 2016). Moreover, the component of Ag may act as an important role upon visible-light illumination (Chen et al., 2015b). For comparison, UV-vis spectra of different samples were investigated. As shown in Fig. 2B, both blank TiO_2 (*curve a*) and TiO_2/NDG (*curve b*) had typical high absorption under UV light. TiO_2/NDG showed a slightly higher visible-light absorption region compared with TiO_2. While the absorption of the TiO_2-Ag/NDG composites (*curve c*) showed wide absorption from UV to visible light/infrared (NIR), which demonstrated that Ag nanocrystals could extend the absorption to visible light/NIR region. To further demonstrate that cathodic photocurrent of TiO_2-Ag/NDG under irradiation wavelength over 450 nm was contributed by Ag nanocrystals, the photocurrent

measurements of different samples were performed (Fig. S3). When the photoelectrodes are excited by UV light, the photon-generated electrons are injected into the conduction band of TiO_2, and leave the holes at the valence band. Due to the band bending, the electrons transfer to the counter electrode through the outer circuit, while the holes are directly involved in the oxidation reaction at the interface of photoelectrode and solution (Chen et al., 2015a; Chen et al., 2015b). Thus, anodic photocurrent is produced on the photoelectrodes. Specifically, n-type semiconductors (e.g. TiO_2) have electrons as the major charge carriers responsible for their conductivity (Nada et al., 2017). Under visible light illumination (> 420 nm), Ag nanocrystals can be excited and while only the photogenerated holes are transferred to the ITO substrate and electrons are involved in the reduction reaction at the Ag NC-electrolyte interface, resulting the negative photocurrent (Chen et al., 2015b). Therefore, it could be concluded that Ag nanocrystals were visible light-responsive photoactive materials, which contributed to the charge-transfer process in generating cathodic photocurrent of TiO_2-Ag/NDG composites (Chen et al., 2015b; Roy et al., 2017). While TiO_2 nanoparticles were regarded as UV-responsive photoactive materials and could generate cathodic photocurrents. With respect to NDG, it made its own contribution to promote the charge-transfer process, prolong the charge carriers lifetime and then enhance the photocurrent intensity. The lifetime in the time-resolved fluorescence decay spectra of TiO_2-Ag/NDG nanocomposite was longer than that of TiO_2-Ag (Fig. S4). It is believed that the increased lifetime of the charge carriers is associated with the improvement of electron transport due to addition of NDG, leading to a lower recombination rate of the electron-hole pairs (Mariserla et al., 2020). All these phenomena indicated that the photocurrent of the as-prepared materials could be controlled via tuning the

wavelengths, which afforded a key prerequisite for the development of the wavelength-switchable PEC sensor.

3.3. Fabrication of the PEC aptasensor

As a proof-of-concept, a PEC aptasensor for detection of CAP and TET was fabricated (Scheme S2A). Briefly, TiO_2-Ag/NDG nanocomposites were firstly coated on the surface of an ITO electrode. Then, two types of aptamers for identifying CAP and TET were patterned and conjugated in the two sensing regions of the nanocomposite-modified electrode to construct a PEC aptamer sensor for detection of two antibiotics CAP and TET concurrently. The mechanism of wavelength-switchable anodic and cathodic photocurrent generation based on TiO_2-Ag/NDG composites was shown in Scheme S2B. The conversion of the analyte binding to the increased photocurrent response could be attributed to the photocatalytic degradation through both oxidation/reduction of CAP and TET molecules captured by aptamer on the electrode surface. Antibiotics including CAP and TET can be degraded by both oxidation and reduction processes (Jeong et al., 2010; Song et al., 2020; Peng et al., 2021; Wang, et al., 2018). Under 380 nm irradiation, mainly photogenerated holes are generated on the nanocomposite-coated working electrode surface, which directly oxidizes adsorbed CAP and TET molecules.

$$CAP/TET + h^+ \rightarrow \text{products}$$

Therefore, some photogenerated holes are consumed and the recombination of photogenerated electron–hole pairs is inhibited, and the left electrons will then be driven to the

counter electrode by the potential to facilitate the generation of an anodic current. Under 600 nm irradiation, only Ag NCs generates photogenerated electrons on the working electrode, which generate hydroxyl radical through the reaction to react with CAP and TET molecules:

$$O_2 + 2H^+ \xrightarrow{e^-} H_2O_2 \xrightarrow{e^-} OH^- + OH^{\cdot}$$

$$CAP/TET + OH^{\cdot} \rightarrow \text{products}$$

Similarly, photogenerated electrons are consumed and the recombination of photogenerated electron–hole pairs is inhibited. The left holes will then be driven to the counter electrode which will facilitate the generation of cathodic current. NDG in the hybrid nanocomposites can enhance charge transfer and prolong the lifetime charge carriers.

The mechanism of the wavelength-regulated switchable photoelectrochemical system for concurrent detection of CAP and TET is shown in Scheme 1. Without target antibiotics, there are no output signals. Since the laser irradiation with 380 nm generates anodic current and the laser irradiation with 600 nm generates cathodic current, the irradiation with both 380 nm and 600 nm with target antibiotics also will not generate output signals. The irradiation with only 380 nm or with only 600 nm in the presence of target antibiotics on the related aptamer functionalized sensing areas will generate the related output signals. By switching the irradiation light wavelengths, anodic currents and cathodic currents on the two sensing areas will be switched accordingly.

The surface microstructure morphology of TiO_2-Ag/NDG nanocomposites-modified ITO electrode was characterized by SEM in Fig. S5A. It could be observed that the surface of the

electrode was covered by a layer of particles. Auger electron spectroscopy (AES) was then used to confirm the composition of the particles. As shown in Fig. S5B, elements of carbon, nitrogen, titanium, silver and oxygen were detected on the surface of the electrode, which was consistent with the XPS results of the TiO_2-Ag/NDG nanocomposites. These results indicated that the nanocomposites were assembled on the surface of ITO electrode successfully. The successful attachment of aptamer has been experimentally demonstrated by electrochemical impedance spectroscopy (EIS). The aptamers were assembled onto the surface of NDG through π–π stacking interaction, which has been widely used in the fields of aptasensing. The conjugated aromatic ring structure of NDG provided an excellent platform for aptamer stable immobilization via π–π stacking interaction (Ge et al., 2018; Jiang et al., 2019). As shown in Fig. S6, with the attachment of aptamer molecules on the TiO_2-Ag/NDG modified electrode (curve b,c), the value of R_{et} was found to be obviously increased. Since aptamer molecules had phosphoric acid skeleton structure, the attachment of aptamer molecules on electrodes were not beneficial for electron transfer, leading to the increase of R_{et} (Malmir et al., 2021). Such phenomenon demonstrated that the aptamer was successfully coated on the surface.

With addition of target antibiotics on the related sensing areas, antibiotics molecules are captured by the related specific aptamers on the sensing area, leading to the change of photocurrents. The stepwise fabrication process of this PEC aptasensor was monitored by measuring the change of photocurrents (Fig. 3). Under illumination at 380 or 600 nm light, the bare ITO electrodes displayed weak photocurrents on the two sensing areas (*curve a* in Fig. 3A and Fig. 3B). When TiO_2-Ag/NDG nanocomposites were coated onto two adjacent sensing areas

on the ITO surface, the photocurrent increased greatly (*curve b* in Fig. 3A and Fig. 3B). After these two sensing areas were functionalized with aptamers specific for CAP and TET, the anodic photocurrent under 380 nm and cathodic photocurrent under 600 nm decreased obviously due to the increased steric hindrance (*curve c* in Fig. 3A and Fig. 3B). When the target CAP and TET molecules were added on the related sensing areas, the targets could be captured by specific aptamers and then consumed the holes in the nanocomposites, leading to the increase of anodic and cathodic photocurrents under illumination of different wavelengths (*curve d* in Fig. 3A and Fig. 3B). Similar to previous reported photocatalytic oxidation reactions for CAP and TET (Liu et al., 2016b; Peng et al., 2021; Wang, et al., 2018), photogenerated holes on electrode surface could directly oxidize adsorbed CAP and TET molecules, or photogenerated electrons could generate hydroxyl radicals ($OH^{\bullet}$) to react with CAP and TET molecules, leading to the photocurrent increase. In order to demonstrate the important roles of hydroxyl radicals ($OH^{\bullet}$) and holes (h^{+}) for photocurrent increase, benzoquinone (BQ), isopropyl alcohol (IPA), and oxalic acid (OA) were used as trapping agents to capture superoxide radicals, hydroxyl radicals ($OH^{\bullet}$), and holes (h^{+}), respectively (Eswar et al., 2016; Adhikari et al., 2019). The photocurrents of the as-fabricated sensor in the absence and presence of the scavengers of BQ, IPA and OA were measured, respectively. As shown in Fig. S7, the photocurrent increased significantly in the control group (a) with the addition of TET or CAP under the light illumination. The effect is neglectable in the presence of superoxide radical scavenger, whereas obvious inhibition of the photocurrent increase was observed in the presence of the radical scavengers of $OH^{\bullet}$ (c) and h^{+} (d) respectively, suggesting that $OH^{\bullet}$ and h^{+} were the major radicals responsible for antibiotics reactions.

In order to prove the versatility of this approach and the validity of the detection mechanism, the reverse aptamer/nanocomposite composition has been studied. Specifically, such proposed PEC sensing strategy was utilized to detect TET under irradiation of 380 nm and CAP under irradiation of 600 nm, respectively. As shown in Fig. S8, after these two sensing areas were functionalized with aptamers specific for TET and CAP, the anodic photocurrent under 380 nm and cathodic photocurrent under 600 nm decreased obviously. When the target TET and CAP molecules were presented in the system, the targets could be captured by specific aptamers and then photodegraded by the nanocomposites, leading to the increase of anodic and cathodic photocurrents under illumination of different wavelengths. The above PEC characterization results could prove the versatility of this approach and the validity of the detection mechanism.

Optimizing parameters involved in the sensor preparation process is of high importance for constructing high-performance PEC aptasensors. The photocurrent signal of the developed sensor could be influenced by the concentration of the aptamers and the binding time between aptamers and target antibiotics. As shown in the Fig. 3C, the anodic and cathodic photocurrents were both increased with the increase of aptamer concentration, and then tended to be constant. The optimal aptamer concentration for CAP assay under 380 nm and TET detection under 600 nm was 1.5 μM and 2.0 μM, respectively. Besides, the influence of the incubation time with the target antibiotics on the photocurrent of PEC sensor was also studied (Fig. 3D). Obviously, with the increase of incubation time, the photocurrent quickly elevated and then reached a plateau after 15 min and 20 min for CAP assay and TET assay, respectively. Therefore, incubation time of 20 min was chosen

for the following antibiotics sensing experiments. The effects of pH and ionic strength on the sensing performance of the aptasensor were then evaluated. As shown in Fig. S9A, the photocurrent amplitude of aptasensor for both CAP and TET detection increased with the increase of pH from 5 to 7.4, and reached its maximum at pH = 7.4. Then the photocurrent signal decreased slightly when the pH further increased. Therefore, pH = 7.4 was selected as the optimal pH value for antibiotics detection. The influence of ionic strength on sensing performance is also tested in different concentrations of PBS solution while keeping the pH constant (Fig. S9B). It could be observed that the photocurrents almost kept constant when the ionic strength was lower than 0.1 mol L^{-1} of PBS solution. When the ionic concentration was larger than 0.1 mol L^{-1} of PBS solution, the photocurrent started to decrease gradually with the increasing of the concentration of PBS. Thus, 0.1 mol L^{-1} PBS solution was selected for the following sensing experiments.

3.4. Sensing performance of wavelength-resolved PEC sensor

To estimate the analytical performance of the wavelength-resolved sensing, the targets CAP and TET with different concentrations were measured by the as-fabricated PEC biosensor. As shown in Fig. 4, the photocurrent intensity showed a concentration-dependent increase for both CAP and TET. The photocurrent intensity showed a linear increase with the logarithm of the CAP concentrations in the range of 50 pM ~ 10 nM, and the limit of detection (LOD) was 16.7 pM under 380 nm illumination (Fig. 4A and 4B). Similarly, the logarithm of the TET concentration was found to have a linear detection range of 0.1 nM to 0.1 mM, with an LOD of 30 pM under

600 nm light irradiation (Fig. 4C and 4D). The comparison results of the obtained detection characteristics with other reported methods have been listed in Table S2, the performance of the proposed aptasensor displayed a wider linear range and a low detection limit at pM level. Moreover, the as-fabricated PEC aptasensor was capable of concurrently detecting CAP and TET via simply regulating the irradiation wavelength. In addition, this fabricated sensor required only simple equipment and a small number of pretreated samples.

3.5. Selectivity, stability and reproducibility

In order to explore the interference effects of TET and CAP on each other on this PEC sensing chip, the cross-reaction test between TET and CAP was performed. Here, 1 nM TET and 1 nM CAP were added to the CAP aptamer-conjugated sensing area and TET aptamer-conjugated sensing area, respectively. As shown in Fig. S10, the addition of 1 nM TET exhibited a negligible photocurrent change on the CAP aptamer-conjugated sensing area under 380 nm. Similarly, the addition of 1 nM CAP did not cause an obvious photocurrent change on TET aptamer-conjugated sensing area under 600 nm. The results demonstrated that the two targets have negligible interference with each other, which could be used for concurrent detection in one chip. Moreover, the selectivity of the as-fabricated PEC sensor was evaluated by incubating with other different kinds of antibiotics including kanamycin, doxycycline, ciprofloxacin, and chlorotetracycline on the sensing areas conjugated with CAP and TET aptamers. Here, the concentrations of target CAP and TET are 5 nM and the concentrations of other antibiotics are 50 nM. As shown in Fig. 5, compared with the target CAP and TET, even if the concentration is 10 times higher, the

photocurrent increase of non-target antibiotics is negligible, which indicates that the manufactured PEC aptamer sensor has good specificity. Such phenomena could be attributed to the good selectivity of CAP and TET aptamers conjugated on the biosensor surface.

To evaluate the stability of the fabricated TiO_2-Ag/NDG PEC aptasensor, the photocurrents were measured during 6 weeks of storage at 4ºC (Fig. S11). The PEC sensor retained about 95.3% (for CAP sensor) and 91.6% (for TET sensor) of its initial photocurrent response, which demonstrated that the developed PEC aptasensor had satisfactory long-term stability. Moreover, the photocurrents with multiple turn-on/turn-off cycles were measured to evaluate the stability of the sensor during multiple measurement cycles (Fig. S12). Obviously, both anodic and cathodic photocurrents were quite stable without obvious change. Moreover, the inter-assay precision of five as-prepared PEC sensors was examined upon the addition of the antibiotics. The relative standard deviations (RSD) of the five measurements were 4.9% and 5.3% for CAP and TET, respectively, suggesting the excellent reproducibility of the PEC sensor.

3.6. The applicability of the biosensor for multiplexed evaluation

The reliability and applicability of the designed PEC biosensor was evaluated by standard addition methods in Yangtze River water and honey samples. The extraction solution was prepared in Experimental section. Different concentrations of antibiotics were spiked into water and honey samples, and the analytical results were presented in Table S3. The recovery rates for CAP detection under 380 nm irradiation were between 94.0 ~ 106.2%. As for TET detection under 600

nm irradiation, the recovery rates were between 96.7 ~ 108.6%. These results indicated that the as-fabricated PEC aptasensor had great potential for detection of two antibiotics concurrently in real samples. Moreover, the performance of the sensor for the analysis of real samples containing multiplexed antibiotics including CAP, TET, kanamycin, doxycycline, ciprofloxacin and chlorotetracycline were investigated. The concentrations of target CAP and TET were 5 nM and the concentrations of other antibiotics were 50 nM. As shown in Table S4, the recovery rates for CAP and TET detection were between 92.8 ~ 98.0%, indicating the as-fabricated PEC sensor could provide a useful tool for detection of two antibiotics concurrently in real samples.

4. Conclusion

In summary, a novel wavelength-dependent PEC aptasensor was designed and fabricated for concurrent sensing of two antibiotics based on hybrid TiO_2-Ag/NDG nanocomposite with high sensitivity, specificity and reliability. The as-fabricated PEC aptasensor could concurrently detect CAP and TET antibiotics via anodic photocurrent and cathodic photocurrent by simply tuning the illumination wavelength. Such proposed PEC aptasensor displayed a good sensing performance with wide linear detection ranges from pM to nM, low detection limit at pM level, good selectivity and reliability. This work represents a significant advancement towards practical PEC applications such as ternary opto-electronics and switchable chemical regulation.

CRediT authorship contribution statement

Ding Jiang: Conceptualization, Methodology, Validation, Writing- original draft. Yude Zhang: Experimental design, Photoelectrochemical measurement. Xiaojiao Du: Writing-review&editing. Youhua Tan: review & editing. Wen Chen: data analysis, Mo Yang: Writing-review & editing, Supervision, Funding acquisition.

Declaration of Competing Interest

The authors declare that they have no known competing financial interests or personal relationships that could have appeared to influence the work reported in this paper.

Acknowledgements

The present work was supported by the National Natural Science Foundation of China (No. 21904014, 21904015, and 31771077), the Natural Science Foundation of Jiangsu Province (BK20190928), the Postdoctoral Science Foundation funded project of Jiangsu Province (2020Z266), the Natural Science Foundation of the Jiangsu Higher Education Institutions of China (19KJB150003), Changzhou Sci & Tech Program (CJ20190059), the Shenzhen-Hong Kong-Macao Science and Technology Plan Project (Category C, SGDX2020110309260000), the Research Grants Council (RGC) of Hong Kong Collaborative Research Grant (C5011-19G), the Research Grants Council (RGC) of Hong Kong General Research Grant (15214619 and 15210818), and the Hong Kong Polytechnic University internal fund (G-YW2H and 1-ZE1E). This work was also supported by the University Research Facility in Life Sciences of the Hong Kong Polytechnic

University.

References

Adhikari, S., Selvaraj, S., Kim, D.H., 2019. Appl. Catal. B-Environ. 244, 11–24.

Antuch, M., Millet, P., Iwase, A., Kudo, A., 2018. Appl. Catal. B-Environ. 237, 401–408.

Bourée, W.S., Prévot, M.S., Jeanbourquin, X.A., Guijarro, N., Johnson, M., Formal, F.L., Sivula, K., 2016. Adv. Mater. 28, 9308–9312.

Brodin, T., Fick, J., Jonsson, M., Klaminder, J., 2013. Science 339, 814–815.

Chen, H.J., Lyu, M.Q., Zhang, M., Feron, K., Searles, D.J., Dargusch, M., Yao, X.D., Wang, L.Z., 2017. ChemSusChem 10, 670–674.

Chen, H.J., Liu, G., Wang, L.Z., 2015a. Scientific Reports 5, 10852.

Chen, H.J., Wang, Q., Lyu, M.Q., Zhang, Z., Wang, L.Z., 2015b. Chem. Commun. 51, 12072–12075.

Chu, Y.X., Han, T.T., Deng, A.P., Li, L.L., Zhu, J.J., 2020. Trends Anal. Chem. 123, 115745.

Dai, H., Zhang, S.P., Hong, Z.S., Lin, Y.Y., 2016. Anal. Chem. 88, 9532–9538.

Deng, H.M., Huang, L.J., Chai, Y.Q., Yuan, R., Yuan, Y.L., 2019. Anal. Chem. 91, 2861–2868.

Durango-Giraldo, G., Cardona, A., Zapata, J.F., Santa, J.F., Buitrago-Sierra, R., 2019. Heliyon, 5, e01608.

Eswar, N.K., Ramamurthy, P.C., Madras, G., 2016. New J. Chem., 40, 3464–3475.

European Union (EU), Commission regulation No. 37/2010, On pharmacologically active substances and their classification regarding maximum residue limits in foodstuffs of animal

origin, Off. J. Eur. Communities: Legis., 2010, 15, 19 – 64.

Furtado, L.F.O., Alexiou, A.D.P., Goncalves, L., Toma, H.E., Araki, K., Angew. Chem. Int. Ed. 2006, 45, 3143-3146.

Ge, L., Li, H.N., Du, X.J., Zhu, M.Y., Chen, W., Shi, T.Y., Hao, N., Liu, Q., Wang, K., 2018. Biosens. Bioelectron. 111, 131–137.

Gilea, D., Radu, T., Muresanu, M., Carja, G., 2018. Appl. Surf. Sci. 444, 407–413.

Jeong, J., Song, W.H., Cooper, W.J., Jung, J., Greaves, J., 2010. Chemosphere, 78, 533-540.

Jiang, D., Yang, C.Q., Fan, Y.D., Leung, H.M.P., Inthavong, K., Zhang, Y., Li, Z.Y., Yang, M. Biosens. Bioelectron. 2021. 183, 113214.

Jiang, D., Du, X.J., Chen, D.Y., Zhou, L., Chen, W., Li, Y.Q., Hao, N., Qian, J., Liu, Q., Wang, K., 2016. Biosens. Bioelectron. 83, 149–155.

Jiang, D., Du, X.J., Liu, Q., Hao, N., Wang, K., 2019. Biosens. Bioelectron. 126, 463–469.

Jiang, D., Du, X.J., Liu, Q., Zhou, L., Qian, J., Wang, K., 2015. ACS Appl. Mater. Interfaces 7, 3093–3100.

Joshi, A., Kim, K.H., 2020. Biosens. Bioelectron. 153, 112046.

Lajin, B., Goessler, W., 2020. Anal. Chem. 92, 9156–9163.

Liu, X.G., Dong, G.J., Li, S.P., Lu, G.X., Bi, Y.P., 2016a. J. Am. Chem. Soc. 138, 2917–2920.

Liu, Y., Yan, K., Zhang, J.D., 2016b. ACS Appl. Mater. Interfaces 8, 28255−28264.

Li, C.H., Zhang, X.S., Wen, S.M., Xiang, R., Han, Y., Tang, W.Z., Yue, T.L., Li, Z.H., 2020a. J. Hazard. Mater. 395, 122615.

Li, Z.K., Wei, Y.Y., Gao, X., Ding, L., Lu, Z., Deng, J.J., Yang, X.F., Caro, J., Wang, H.H., 2020b. Angew. Chem. Int. Ed. 59, 9751–9756.

Loget, G., Li, G.Z., Fabre, B., 2015. Chem. Commun. 51, 11115-11118.

Malmir, M., Arjomandi, J., Khosroshahi, A.G., Moradi, M., Shi, H., 2021. Biosens. Bioelectron. 189, 113356.

Mariserla, B.M.K., Alee, K.S., Kasthuri, S., Gawas, P., Rao, D.N., Nutalapati, V., 2020. Opt. Mater. 109, 110366.

Martin, J.K., Sheehan, J.P., Bratton, B.P., Moore, G.M., Mateus, A., Li, S.H.J., Kim, H., Rabinowitz, J.D., Typas, A., Savitski, M.M., Wilson, M.Z., Gitai, Z., 2020. Cell 181, 1518–1532.

Matsui, J., Mitsuishi, M., Aoki, A., Miyashita, T., 2004. J. Am. Chem. Soc. 126, 3708–3709.

Nada, A.A., Nasr, M., Viter, R., Miele, P., Roualdes, S., Bechelany, M., 2017. Journal of Physics Chemistry C. 121, 24669-24677.

McConnell, E.M., Nguyen, J., Li, Y.F., 2020. Front. Chem. 8, 434.

Peng, B., Lu, Y., Luo, J., Zhang, Z.L., Zhu, X., Tang, L., Wang, L.L., Deng, Y.C., Ouyang, X.L., Tan, J.S., Wang, J.J., 2021, J. Hazard. Mater. 401, 123395.

Qian, J., Cui, H.N., Lu, X.T., Wang, C.Q., An, K.Q., Hao, N., Wang, K., 2020. Chem. Eng. J. 401, 126017.

Roy, S., Basu, K., Gayen, K., Panigrahi, S., Mondal, S., Basak, D., Banerjee, A., 2017. J. Phys. Chem. C 121, 5428–5435.

Shah, M.S.A.S., Zhang, K., Park, A.R., Kim, K.S., Park, N.G., Park, J.H., Yoo, P.J., 2013.

Nanoscale 5, 5093–5101.

Shi, J.Y., Lyu, J., Tian, F., Yang, M., 2017. Biosens. Bioelectron. 93, 182-188.

Song, X.Z., Huang, D., Zhang, L., Wang, H., Wang, L.Y., Bian, Z.Y. 2020. Electrochimica Acta, 330, 135187.

Szacilowski, K., Macyk, W., Stochel, G., 2006. J. Am. Chem. Soc. 128, 4550-4551.

Temerov, F., Pham, K., Juuti, P., Mäkelä, J.M., Grachova, E.V., Kumar, S., Eslava, S., Saarinen, J.J., 2020. ACS Appl. Mater. Interfaces 12, 41200–41210.

Wang, D.B., Jia, F.Y., Wang, H., Chen, F., Fang, Y., Dong, W.B., Zeng, G.M., Li, X.M., Yang, Q., Yuan, X.Z., 2018. J. Colloid Interface Sci. 519, 273–284.

Wang, L.N., Ma, W.G., Gan, S.Y., Han, D.X., Zhang, Q.X., Niu, L., 2014. Anal. Chem. 86, 10171–10178.

Wang, J., Liu, Z.H., Hu, C.G., Hu, S.S., 2015. Anal. Chem. 87, 9368–9375.

Wang, J., Long, J., Liu, Z.H., Wu, W.Z., Hu, C.G., 2017. Biosens. Bioelectron. 91, 53–59.

Wen, Y.Y., Ding, H.M., Shan, Y.K., 2011. Nanoscale 3, 4411–4417.

Wu, Z.S., Yang, S.B., Sun, Y., Parvez, K., Feng, X.L., Müllen, K., 2012. J. Am. Chem. Soc. 134, 9082–9085.

Ye, W.W., Guo, J.B., Bao, X.F. Chen, T., Weng, W.C., Chen, S., Yang, M. 2017. Materials 10, 603.

Zhao, Y.F., Jia, X.D., Chen, G.B., Shang, L., Waterhouse, G.I.N., Wu, L.Z., Tung, C.H., O'Hare, D., Zhang, T.R., 2016. J. Am. Chem. Soc. 138, 6517–6524.

Zhou, Z., Hao, N., Zhang, Y., Hua, R. Qian, J., Liu, Q., Li, H.N., Zhu, W.H., Wang, K., 2017.

520 Chem. Commun. 53, 7096-7099.

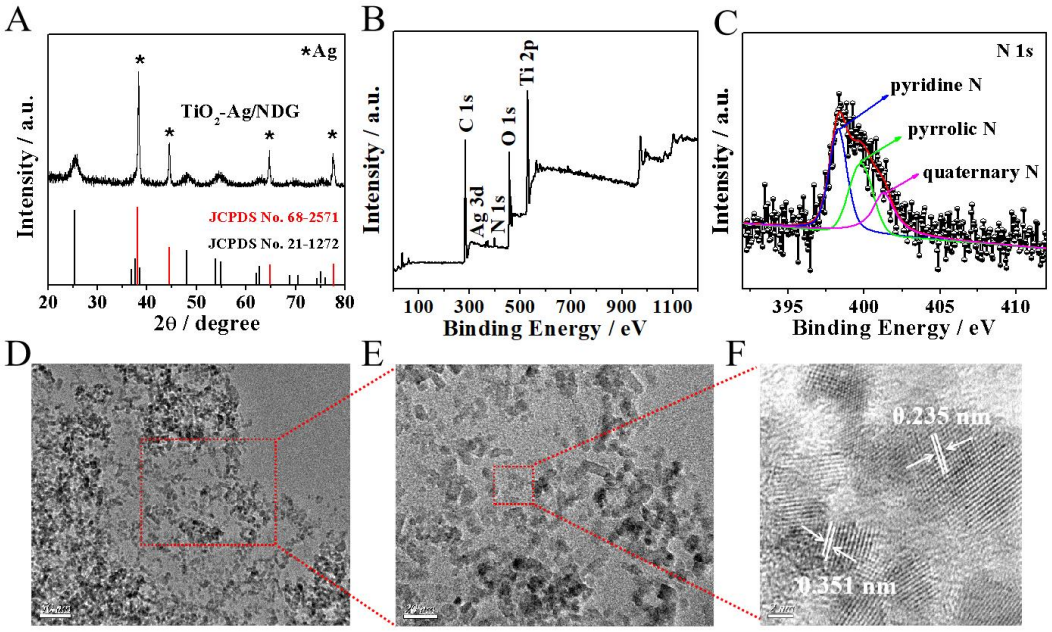

Fig. 1. (A) XRD patterns of JCPDS No. 21-1272, No. 68-2571 and TiO_2-Ag/NDG; (B) XPS survey spectra of the as-prepared TiO_2-Ag/NDG; (C) High-resolution XPS spectra of the N 1s in the as-prepared composites. (D) TEM image of the as-prepared TiO_2-Ag/NDG; (E) High-magnification TEM image of TiO_2-Ag/NDG. (F) Lattice fringes in the composites.

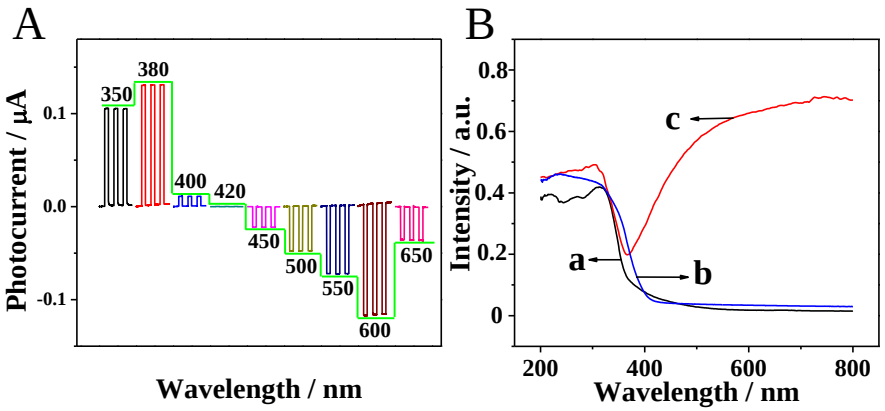

535

Fig. 2. (A) Photocurrent response of the TiO_2-Ag/NDG nanocomposites under different illumination wavelengths (from 350 nm to 650 nm); (B) UV-vis diffuse reflectance spectroscopy of the TiO_2 (curve a), TiO_2/NDG (curve b) and TiO_2-Ag/NDG (curve c).

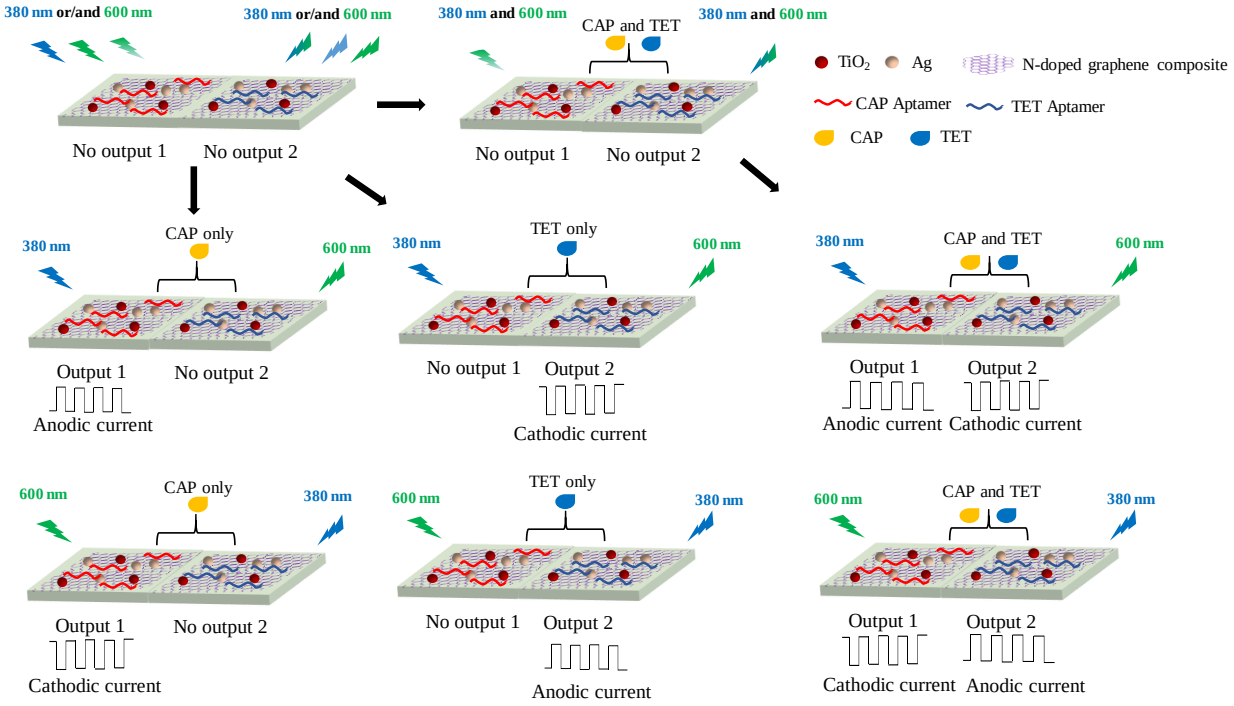

Scheme 1. The mechanism of anodic and cathodic photocurrent generation on the aptamer functionalized TiO_2-Ag/NDG photoelectrode for CAP and TET sensing.

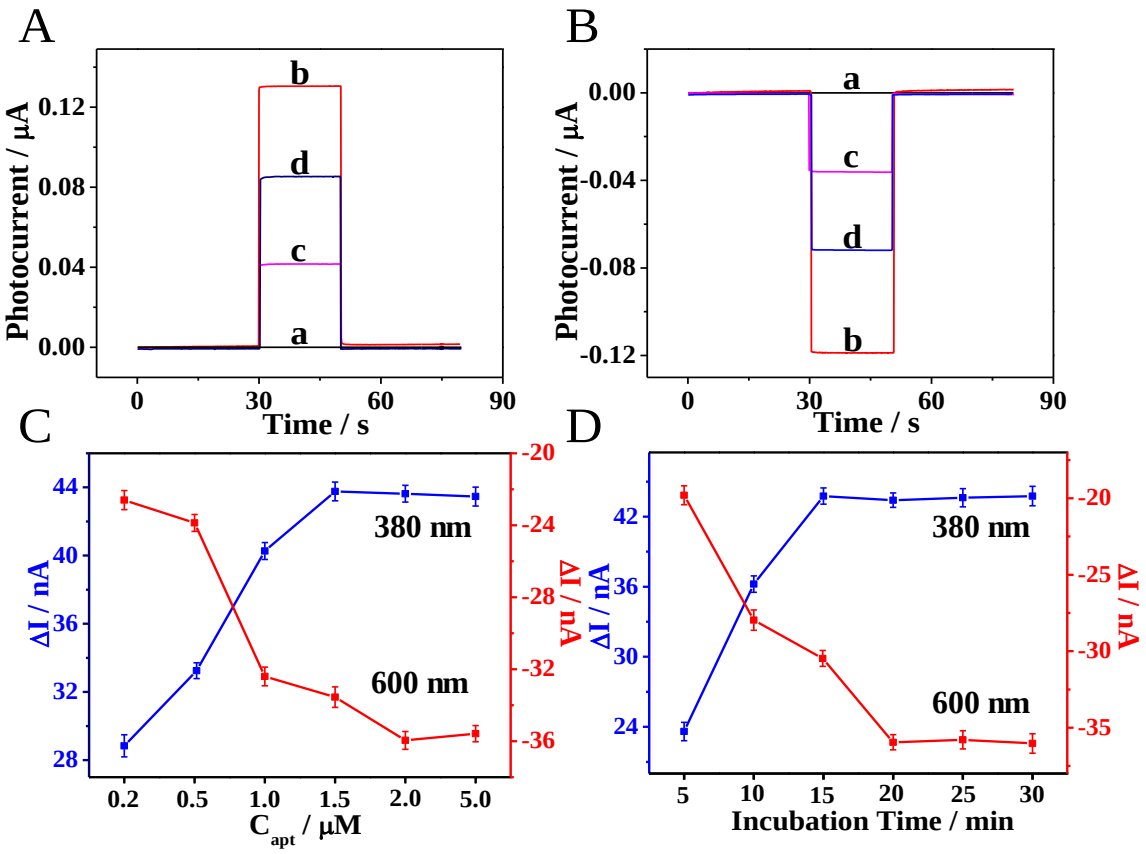

Fig. 3. Characterization of PEC response in the fabrication process of the PEC aptasensor. (A) Under light with 380 nm: bare ITO (curve a), TiO_2-Ag/NDG/ITO (curve b), aptamer-TiO_2-Ag/NDG/ITO (curve c), and 1 nM CAP captured by aptamer-TiO_2-Ag/NDG/ITO (curve d); (B) Under irradiation with 600 nm: bare ITO (curve a), TiO_2-Ag/NDG/ITO (curve b), aptamer-TiO_2-Ag/NDG/ITO (curve c), and 5 nM TET captured by aptamer-TiO_2-Ag/NDG/ITO (curve d); Photocurrent responses of the two sensing areas of the PEC aptasensor (C) with different CAP and TET aptamer concentrations or (D) different incubation time in the presence of targets under the light of 380 nm and 600 nm, respectively. (ΔI is the photocurrent response difference in the presence or absence of CAP or TET; CAP aptamer and TET aptamer concentrations in (D) are 1.5 μM and 2.0 μM, respectively).

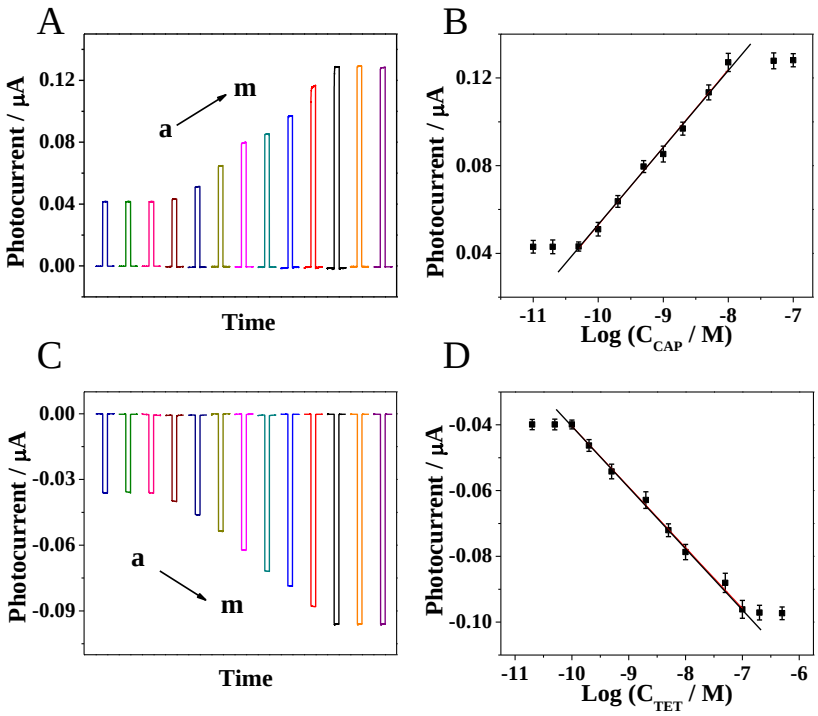

Fig. 4. Photocurrent responses of the PEC aptasensor toward different concentrations of CAP (0.01 ~ 100 nM) (A) and different concentrations of TET (0.01 ~ 500 nM) (C). The corresponding calibration curves with logarithm of CAP concentrations (B) and TET concentrations (D).

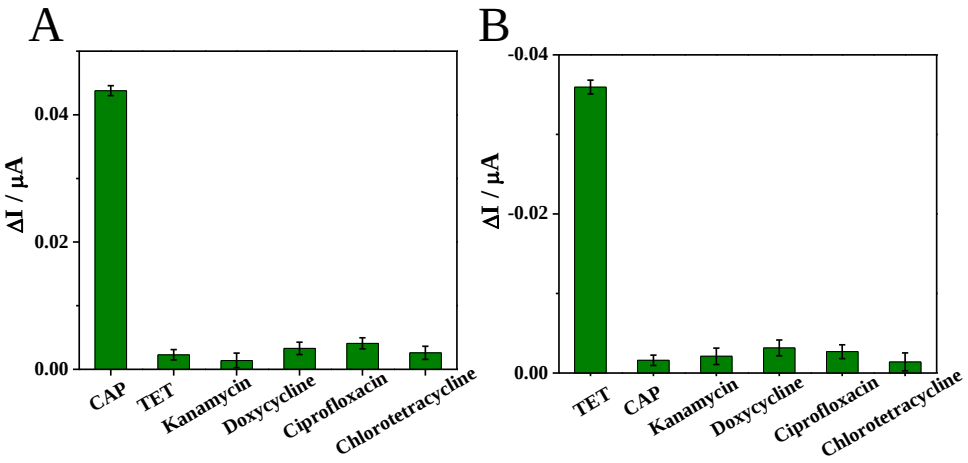

Fig. 5. Selectivity of the PEC aptasensor for CAP (A) and TET (B) detection over other non-target antibiotics (CAP: 5 nM; TET: 5 nM; other interferents: 50 nM).